Indian Journal of Pure & Applied Physics
Vol. 64, July 2026, pp. 707-720
DOI: 10.56042/ijpap.v64i7.27354

Influence of Gd Substitution on the Crystal and Defect Structure of $BaTi_{0.965}Sn_{0.035}O_3$ Ceramics

Kanika Poonia[a], R S Kundu[a*], Neetu Ahlawat[a], Aryan Singh Lather[b], Rinku Singroha[c], Rajesh Parmar[d] & Vinay Kumar[e]

[a]Department of Physics, Guru Jambheshwar University of Science and Technology, Haryana 125 001, India
[b]Ballistics Division, Forensic Science Laboratory, Madhuban, Haryana 132 037, India
[c]Department of Research and Development, Jindal Stainless Limited, Haryana 125 005, India
[d]Department of Physics, Maharshi Dayanand University, Haryana 124 001, India
[e]Department of Physics, College of Basic Science and Humanities,
Chaudhary Charan Singh Haryana Agricultural University, Hisar, Haryana 125 004, India

Received: 7th January 2026; accepted: 8th May 2026

Polycrystalline $Ba_{1-x}Gd_xTi_{0.965}Sn_{0.035}O_3$ (x = 0.00, 0.025, 0.05, 0.075) ceramics were synthesised via a solid-state route to investigate the effect of Gd^{3+} on the structural and microstructural properties of barium tin titanate (BTS). X-ray diffraction (XRD), supported by Rietveld refinement, confirmed a well-crystallised orthorhombic phase (Amm2) with systematic peak shifts indicating successful Gd incorporation. In contrast, a pyrochlore-type $Gd_2Ti_2O_7$ secondary phase appeared at higher Gd contents ($0.025 > x \geq 0.05$), marking the solubility limit. Williamson– Hall Plots showed that Gd doping reduces lattice strain while preserving long-range crystallinity. Electron-density contour and 3D Fourier maps revealed a periodically ordered lattice with subtle local rearrangements induced by Gd^{3+}. FTIR spectra evidenced Ti–O vibrational modes alongside the disappearance of carbonate-related bands. The grain size, as calculated from FESEM micrographs, decreases from 0.721 µm to 0.289 µm due to the solute drag mechanism and the emergence of a secondary phase. Energy-dispersive spectroscopy confirms the elemental makeup of the synthesized samples. Raman spectroscopic analysis agrees well with the XRD studies. These structural and microstructural modifications establish a strong foundation for subsequent investigations into the enhanced dielectric and ferroelectric properties of Gd-modified BTS, highlighting its potential as a lead-free material for advanced capacitors, actuators, sensors, and energy-storage devices.

Keywords: Barium titanate stannate, Rietveld refinement, Ceramics, X-ray diffraction

1 Introduction

In the early 1970s, Smolensky[1] investigated barium stannate titanate (BTS) ceramics as a model system for ferroelectrics exhibiting diffuse phase transitions. It has long served as a cornerstone in the field of ferroelectric and dielectric materials, owing to their perovskite crystal structure and excellent functional properties. Barium Titanate ($BaTiO_3$) is still the most researched of them[2]. However, it can be modified to produce materials with different, and often better, dielectric, ferroelectric, and structural properties by partially substituting Sn^{4+} for Ti^{4+}. A prospective lead-free substitute for capacitors, actuators, sensors, thermistors, and energy storage devices is the resultant chemical, barium tin titanate (BTS)[3].

In BTS ceramics, doping is an effective way to precisely modify their ferroelectric, dielectric, and structural properties. One can intentionally perturb the perovskite lattice, such as altering octahedral tilting, lattice distortion, and the tolerance factor, by carefully swapping cations at either the A-site (Ba^{2+}) or the B-site (Ti^{4+}/Sn^{4+}). Such disturbances cause significant variations in crystal symmetry, phase transitions, and transition temperatures, and these variations are of prime importance to the dielectric response and device performance[4]. Optimizing these fundamental properties of materials using compositional techniques makes it possible to devise BTS ceramics with tailored functional properties, higher thermal and electric field stability, and improved usage in next-generation ferroelectric and dielectric devices[5,6].

A number of polymorphic phase transitions in barium stannate titanate provide a basis for understanding complex phenomena. Developing this topic, an elaborate study on the ferroelectric and dielectric properties, elucidating a phenomenon of phase transformation[7] was performed. To support the preparation, development, and high-field dielectric

*Corresponding author: E-mail: rskundu2007@gmail.com

properties of BTS ceramics, a set of research works was conducted, focusing on diffuse phase transitions and relaxor-like behaviour[8–10]. In addition, research works focused on amphoteric Dy [11], Yb_2O_3 [12], Er^{3+}/Yb^{3+} co-doping [13], even some recent research works based on rare-earth modified BTS by the addition of Nd^{3+}, Er^{3+}, Sm^{3+}, Y^{3+} ions and $BiYO_3$[14–21] into BTS ceramics, they possess an ability to offer variable structural, dielectric, and ferroelectric properties, making them promising lead-free multifunctional materials for advanced electric and energy storage applications[22].

Despite the vast body of literature on bulk barium titanate capacitors, relatively few studies have explored the compositional engineering of BTS ceramics. This work seeks to fill this gap by synthesizing barium stannate titanate and incorporating gadolinium oxide (Gd_2O_3) to investigate the effects of doping with the rare-earth element gadolinium, an amphoteric dopant, on the structural and microstructural properties of BTS ceramics. The primary contribution of this manuscript lies in its exploration of the strategic doping of gadolinium (Gd^{3+}) into BTS ceramics, the subject that has not been addressed in the extant literature. By precisely incorporating Gd^{3+} ions in the perovskite structure of BTS, it has been demonstrating significant modification in the material's structural and microstructural characteristics. The doping of Gd^{3+} leads to a notable reduction in stacking faults, lattice microstrain, and dislocation density, all of which contribute to the formation of larger crystallites and enhanced structural cohesion.

The current study focuses on the preparation of gadolinium-doped $Ba(Ti_{1-x}Sn_x)O_3$ (BTS) ceramics and on a systematic investigation of their structural variations. From the close observation of XRD patterns, some significant crystallographic parameters like crystallite size, lattice micro-strain, stacking faults and dislocation density are calculated to find the impact of Gd incorporation on BTS lattice. To gain a deeper understanding of the lattice distortions and defect structures induced by gadolinium doping, these findings have been further verified and quantified using Williamson–Hall plots. Electron density maps, FESEM micrographs, FTIR and Raman spectra were used in order to further elucidate the gadolinium doped BTS ceramics and validate the XRD results.

This work not only contributes to the understanding of the fundamental properties of BTS ceramics but also lays the groundwork for further research into the enhancement of their performance through compositional engineering. The findings are expected to stimulate further exploration in the domain of barium titanate stannate-based ceramics, offering new avenues for future advancements in the field.

2 Experimental Procedure

High-purity analytical reagent-grade chemicals were used to ensure stoichiometric and chemical purity of the final compositions. Barium carbonate ($BaCO_3$, 99.9 %, Sigma-Aldrich), tin(IV) oxide (SnO_2, 99.996 %, Thermo Fisher Scientific), titanium dioxide (TiO_2, 99 %, Himedia), and gadolinium oxide (Gd_2O_3, 99.9 %, Himedia) were employed as the source materials. The respective weights of the materials corresponded to the stoichiometric ratio of $Ba_{1-x}Gd_xTi_{0.965}Sn_{0.035}O_3$. Wet mixing of the materials was conducted in ethanol using an agate mortar and pestle. The slurry was homogenized for about 6 hrs to facilitate intimate mixing, enhance the dispersion of particles, and minimize microscopic compositional inhomogeneities. Wet grinding assisted with ethanol was performed to improve the homogeneity of the powder mixture and suppress hard agglomeration, thereby enabling more efficient solid-state diffusion during subsequent thermal treatments.

The homogenized mixtures were dried and thermally calcined at 1250 °C for 3 hrs in a high-temperature furnace to trigger the solid-state reactions for the formation of the perovskite phases. The calcined powders were then manually ground to disintegrate the existing agglomerates. A small amount of Polyvinyl Alcohol (PVA), acting as a binder, was added to facilitate the formation of pellets. The mixtures were then pressed into pellets using a hydraulic press to get the green compacts. This provided the mechanical strength to the green compacts.

To densify and improve the crystal structure, the green pellets were sintered at 1350 °C for 1 hour. For ease of description, the compositions will be identified by the following notation: BTS ($BaTi_{0.965}Sn_{0.035}O_3$), G25 ($Ba_{0.975}Gd_{0.025}Ti_{0.965}Sn_{0.035}O_3$), G50 ($Ba_{0.950}Gd_{0.05}Ti_{0.965}Sn_{0.035}O_3$), and G75 ($Ba_{0.925}Gd_{0.075}Ti_{0.965}Sn_{0.035}O_3$). After sintering, selected pellets were finely ground back into powder form for structural characterization such as XRD, Raman and FTIR spectroscopy.

XRD measurements were carried out on a Rigaku Miniflex 2 diffractometer (Japan) with Cu Kα radiation (λ = 1.5405 Å), operated at 30 kV and 15 mA. The diffraction patterns were acquired in 2θ-scan

mode and the acquisition conditions were optimized to obtain high-resolution data suitable for both phase identification and detailed structural refinement. Measured profiles were analyzed by rietveld refinement using the FullProf Suite to accurately determine lattice parameters, crystal symmetry, and fractions of phases. An orthorhombic perovskite structure with space group Amm2 provided the best fit to the experimental data among the tested crystallographic models, as evidenced by the lowest residuals and the highest correlation between observed and calculated intensities for both undoped and Gd-doped BTS compositions.

Apart from the determination of phase and symmetry, a complete line profile analysis of the XRD patterns was carried out to assess the essential microstructural parameters, such as the crystallite size (D), lattice microstrain (ε), probability of stacking faults (α), and dislocation density (ρ), of the synthesized ceramics. The parameters mentioned above are essential for gaining quantitative indications of the crystallization, strain distribution, and defect structure of the synthesized ceramic materials. The morphology of the synthesized materials was analyzed by high resolution field-emission scanning electron microscopy (JSM-7610F Plus) equipped with an energy-dispersive X-ray detector. Room temperature Raman analysis was performed by Alpha 300 WITec microscope with an argon-ion laser of wavelength 532 nm as the excitation source. The transmission IR data of the processed materials were recorded by PerkinElmer Spectrum FTIR software version 10.6.2.

3 Results and Discussion

3.1 Crystal Structure of BTS and Gd-doped BTS Ceramics

In the X-ray diffraction analysis, the XRD patterns of the BTS and Gd-doped BTS ceramics with Gd content of x = 0.0, 0.025, 0.05, and 0.075 are presented in the Fig. 1 (a). In all the samples, strong and sharp peaks corresponding to the Bragg reflections are observed, inferring the presence of a crystalline perovskite structure, thus the inclusion of Gd did not affect the overall lattice of the BTS ceramics. A clear secondary phase peak is absent in the G25 sample, suggesting that the Gd^{3+} ions were fully incorporated into the lattice to give a homogenous solid solution. This is a clear indication that Gd can be substituted for A-site cations in the perovskite lattice to avoid structural instability.

On the other hand, the G50 and G75 samples exhibit additional faint diffraction peaks, denoted by asterisks in Fig. 1 (a). These diffractions can be ascribed to the appearance of a $Gd_2Ti_2O_7$ pyrochlore phase[23] signifying the occurrence of a secondary phase as a consequence of overstepping the native solubility limit of Gd itself within the BTS host matrix. The appearance of the pyrochlore phase indicates a condition where beyond 5 mol % of Gd itself, there are no further lattice sites available for solid-state dissolution of additional Gd^{3+} ions. Instead, it suggests the formation of Gd_2O_3 during sintering with TiO_2 to form a thermodynamically stable $Gd_2Ti_2O_7$ pyrochlore complex[24]. The appearance of such secondary pyrochlore phases of type $R_2Ti_2O_7$ has long been observed within perovskite ceramics with rare-earth dopants such as Dy, Er, Eu, Y, and Ho beyond their individual native solubility limits [14, 25–28], indicating a similar compositional trend throughout the rare-earth series.

Moreover, the greater enhancement of these peaks at higher Gd concentrations further validates the formation of this secondary phase at higher dopant concentrations. This is due to an increase in the proportion of the excess Gd_2O_3 that cannot be

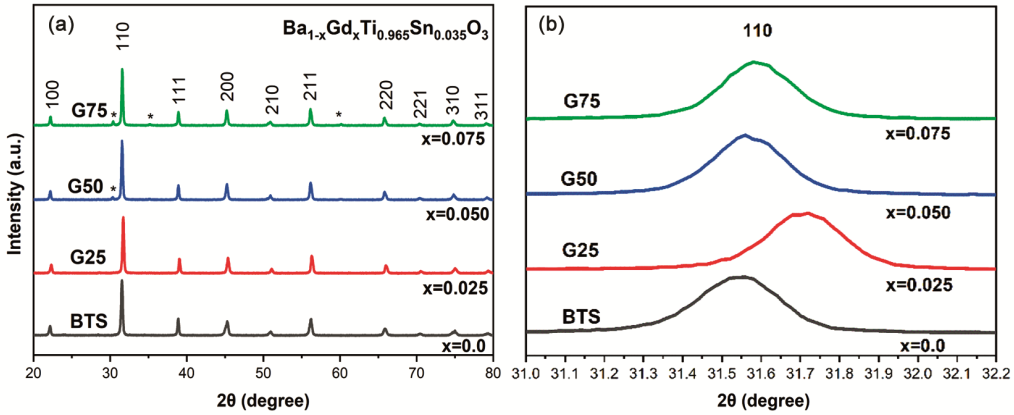

Fig. 1 — (a) XRD pattern of the $Ba_{1-x}Gd_xTi_{0.965}Sn_{0.035}O_3$ with x=0.0, 0.025, 0.05, 0.075 and (b) Magnified view of the prominent peak 110

accommodated in the perovskite structure. Hence, it is clearly visible from the XRD observations that the solubility limit of Gd exists between x = 0.025 and 0.05 within the BTS lattice.

Figure 1 (b) illustrates the enlarged spectrum of the prominent peak 110 for all the synthesized samples. The position of the peak corresponding to sample G25 moves to higher angles because of the shorter radius (0.938 Å) of the Gd^{3+} ion compared to the Ba^{2+} ion (1.35 Å), thus the decrease in the lattice unit cell volume, as depicted in Table 1. The peak for the G50 sample overlaps with the peak of the BTS sample, and the diffraction peak of the G75 also appears close to the BTS peak because of the solubility limit that triggered at x= 0.050. The Table 2 illustrates a comparison of previously reported BTS-based ceramics with the present work.

3.2 Rietveld Refinement of BTS and Gd-doped BTS Ceramics

A detailed structural analysis was carried out for the prepared samples using Rietveld refinement implemented in the FULLPROF Suite. Rietveld refinement is a structural modelling method that can be used to accurately match the real crystal structure. The refinement was performed using the orthorhombic phase and the Amm2 space group for all the samples, indicating that the presence of Gd does not cause the structure to enter other phases. Rietveld refinement plots for the BTS, G25, G50, and G75 samples are given in Fig. 2.

Peak fitting was performed using a Pseudo-Voigt profile, with selected background points used to model the baseline. The background contribution was refined using linear interpolation with movable background heights. First, the scale factor, lattice parameters (a, b, and c), and angular parameters (α, β, and γ) were refined in a methodical order. The overall B factor, background, atomic locations, site occupancies, and peak-related parameters, such as preferred orientation, full width at half maximum (FWHM), and peak-shape coefficients, were then refined. Every atomic parameter was fine-tuned separately. The shift and profile parameters were then changed, and the lattice and atomic parameters were simultaneously refined to evaluate their mutual variations[29]. Table 1 compiles the refined lattice parameters and the statistical measures of refinement quality, which include the goodness-of-fit parameter (χ^2), the residual factor (R_p), and the weighted residual factor (R_{wp}). As illustrated in Fig. 2 (a–d), the difference between the calculated and observed intensities ($Y_{obs} - Y_{cal}$) was used further to assess the quality of refinement and sample preparation. The robustness of the refining process is reflected in the comparatively low values of R_p, R_{wp}, and χ^2, which also confirm that the synthesised samples show excellent structural agreement with the suggested model.

3.3 Structural Parameters of BTS and Gd-doped BTS Ceramics

To perform a comprehensive structural analysis, the synthesized sample's X-ray diffraction (XRD) patterns were carefully examined. These diffraction profiles were used to carefully extract critical metrics such as crystallite size (D), stacking fault probability (α), lattice microstrain (ϵ), and dislocation density (ρ).

Table 1 — Rietveld refinement of the XRD patterns yielded structural features for BTS, G25, G50, and G75, indexed in the orthorhombic (Amm2) phase

Sample ID	Cell parameters	Atoms	Position Co-ordinates			Profile R factors		
			X	y	z	R_{wp}	R_p	χ^2
BTS (x=0.0)	a= 3.9969 (20) Å	Ba	0.0000	0.0000	0.0260 (2)			
	b= 5.6842 (3) Å	Ti/Sn	0.5000	0.0000	0.4963 (2)			
	c=5.6725 (4) Å	O1	0.0000	0.0000	0.4505 (2)	11.8	8.98	4.62
	Vol= 128.877 (13) $Å^3$	O2	0.5000	0.2408 (7)	0.3161 (2)			
G25 (x= 0.025)	a= 4.00301 (2) Å	Ba/Gd	0.0000	0.0000	0.0161 (19)			
	b= 5.67047 (7) Å	Ti/Sn	0.5000	0.0000	0.5021 (19)			
	c= 5.663459 (7) Å	O1	0.0000	0.0000	0.4956 (19)	13.1	10.4	5.74
	Vol= 128.554 (19) $Å^3$	O2	0.5000	0.2542 (8)	1.2618 (19)			
G50 (x=0.05)	a= 4.0208 (3) Å	Ba/Gd	0.0000	0.0000	0.1266 (13)			
	b= 5.6688 (13) Å	Ti/Sn	0.5000	0.0000	0.5218 (13)			
	c= 5.6663 (12) Å	O1	0.0000	0.0000	0.4690 (13)	11.1	8.27	4.77
	Vol= 129.152 (4) $Å^3$	O2	0.5000	0.2479 (9)	1.2379 (13)			
G75 (x= 0.075)	a= 4.0230 (3) Å	Ba/Gd	0.0000	0.0000	0.0126 (3)			
	b=5.6771 (3) Å	Ti/Sn	0.5000	0.0000	0.5218 (3)	11.7	8.29	5.77
	c=5.6760 (3)	O1	0.0000	0.0000	0.4690 (3)			
	ÅVol= 129.640 (12) $Å^3$	O2	0.5000	0.2435 (10)	1.2379 (3)			

Table 2 — A comparison of previously reported BTS-based ceramics with the present work

S. No.	Sample	Method of Preparation	Calcination Temperature	Sintering Temperature	Phase	Space Group	Grain Size	Ref.
1	$Ba_{1-3x/2}Dy_x(Ti_{0.85}Sn_{0.15})O_3$	Solid state reaction	1100 °C for 2hrs	1300-1450 °C for 4 hrs	Cubic	Pm̄3m	10-3µm	11
2	$BaTi_{0.9}Sn_{0.1}O_3 + Er^{3+}/Yb^{3+}$	sol-gel method	1050 °C for 4hrs	-	Tetragonal	P4mm	0.031- 0.052 µm	13
3	$BaSn(_{0.1}Ti_{0.9})O_3$	Solid state reaction	1300 °C for 5hr	1450 °C for 5hr	orthorhombic + Cubic	Amm2 & Pm$\bar{3}$m	-	15
4	$Ba_{1-y}Er_ySn_{0.06}Ti_{0.94}O_3$	Solid state reaction	1200 °C for 3 h	1350 °C for 5 h	Orthorhombic + tetragonal	Amm2 & P4mm	9-25 µm	16
5	$Ba_{1-x}Sm_xTi_{0.965}Sn_{0.035}O_3$	Solid state reaction	1250 °C for 3 h	1350 °C for 1 h	Orthorhombic	Amm2	0.46-0.7 µm	17
6	Y_2O_3-doped BTS	Solid state reaction	1080 °C for 2h	1300 °C for 2hr	Tetragonal	P4mm	0-	18
7	$(Nd_{2x3}Ba_{1-x})(Ti_{0.95}Sn_{0.05})O_3$	Solid state reaction	950 °C for 4 h	1300 °C for 4 h	Tetragonal	P4mm	0.5–2 µm.	19
8	$Ba_{1-1.5x}Y_xTi_{1-z}Sn_zO_3$	Solid state reaction	1200 °C for 3hrs	1300 °C for 3 hrs	Tetragonal, Cubic	P4mm, Pm̄3 m	1.35-6.25 µm	20
9	$(1-x)Ba(Ti_{0.93}Sn_{0.07})_3-xBiYO_3$	Solid state reaction	1320 °C for 4hrs	1280-1320 °C for 2-4 hrs	Orthorhombic, Tetragonal, Tetragonal + Cubic	Amm, P4mm, Pm̄3 m	0.6-1.7 µm	21
10	$Ba_{1-x}Gd_x Ti_{0.965}Sn_{0.035}O_3$	Solid state reaction	1250 °C for 3hrs	1350 °C for 1 hr	Orthorhombic	Amm2	0.289-0.721 µm	Present work

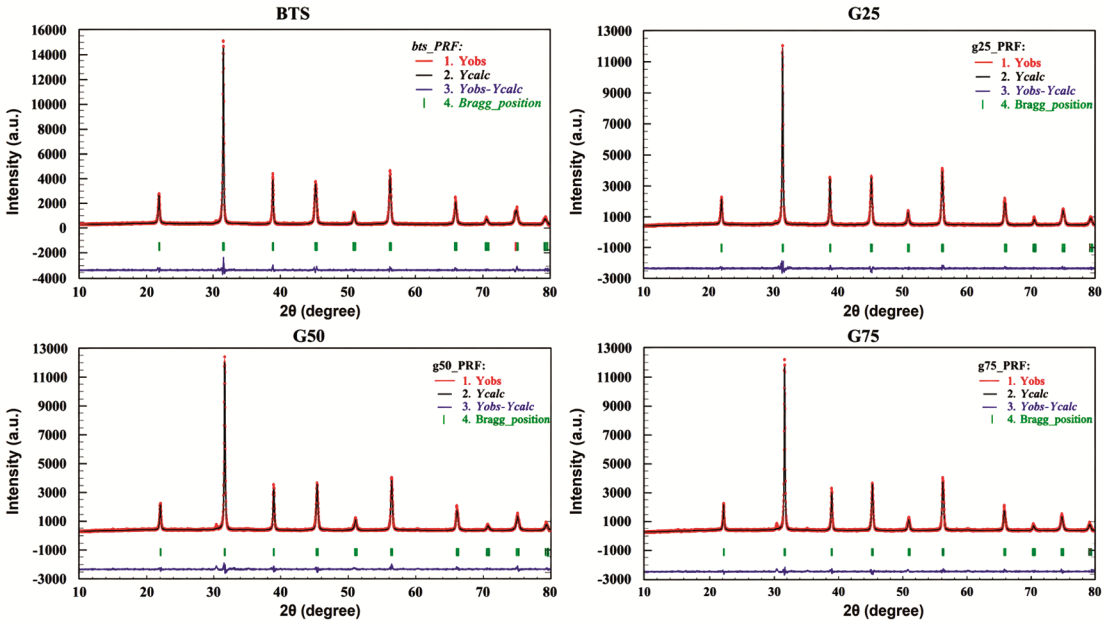

Fig. 2 — Displays the XRD patterns for BTS, G25, G50, and G75 after Rietveld refinement. The red circles represent the empirically observed data, the computed pattern is represented by the black solid line, and the difference between the simulated and observed curves is shown by the blue solid line

These metrics, which provide insights into the defect structure, internal strain distribution, and overall crystallographic coherence, enable a deeper understanding of the influence of synthesis conditions on the materials' structural integrity and defect landscape.

The average size of the small, uniformly ordered regions inside a solid where the crystal lattice remains continuous is known as crystallite size, and it is represented by the letter D. These regions act as single coherent domains during X-ray diffraction. Crystallite size is typically smaller than the overall

particle size, since one particle may contain several such ordered domains. It is estimated from the broadening of XRD peaks, and in this study, the Debye–Scherrer equation was employed to determine it.

Debye-Scherrer equation $D = \frac{0{\cdot}9\,\lambda}{\beta\,cos\,\theta}$ … (1)

where β is the full width at half maximum (FWHM) of the diffraction peaks in radians, θ is the Bragg's angle, and λ represents the X-ray wavelength, specifically that of the Cu K_α radiation (1.5405 Å).

As presented in Table 3, the crystallite size increases from 26 nm in the undoped BTS to 28 nm in the most highly Gd-doped composition. This progressive enlargement indicates that gadolinium incorporation facilitates grain-growth processes within the BTS ceramic matrix, thereby promoting the formation of larger and more refined crystallites[30].

A stacking fault (α) is a planar crystallographic defect characterized by a local disruption in the regular stacking sequence of atomic planes within a crystal lattice. The mechanical, electrical, and optical properties of the material can be significantly affected by these defects, which often occur during crystal growth, mechanical deformation, or the addition of dopants or impurities. It can be calculated using the Eq. (2).

$$\alpha = \frac{2\Pi^2 * \beta}{45(3\,tan\,\theta)^{1/2}} \quad \ldots (2)$$

As evident from Table 3, the addition of Gd to the BTS lattice reduces the stacking fault. This decrease implies that Gd inclusion inhibits stacking fault formation, leading to a more structurally refined and ordered crystal lattice.

When dopant ions are integrated into the host structure, a crystal lattice experiences small, localized distortions known as lattice microstrain, denoted by ϵ. The introduction of these replacement ions causes small changes in interatomic spacing because they usually have different ionic radii, valence states, or coordination environments from those of the ions they replace. Internal stress fields produced by these changes result in non-uniform, dispersed strain throughout the lattice. In general, the lattice's structural adaptation to accommodate ions of mismatched size or charge is reflected in the microstrain associated with dopant incorporation. The following formula is used to quantify this effect, which often appears as X-ray diffraction peak broadening.

$$\epsilon = \frac{\beta\,cot\,\theta}{4} \quad \ldots (3)$$

Lattice microstrain clearly decreases as Gadolinium content increases (Table 3), from 0.00343 in undoped BTS to 0.00318 in G25, 0.00320 in G50, and 0.00313 in G75. This decrease implies that Gd inclusion reduces internal lattice strain, leading to a less distorted, more relaxed crystal structure. The reduction in microstrain suggests that Gd ions are effectively incorporated into the lattice, enhancing structural homogeneity and minimizing defects. These results show how Gd improves the crystallographic integrity and stabilizes the BTS lattice.

The dislocation density (ρ), which indicates the degree of internal strain and lattice defects in the crystal structure, is the number of dislocations in a unit volume of the material. Variations in dislocation density can significantly alter a material's structural, mechanical, and electrical properties. The following formula can be used to calculate it.

$$\rho = \frac{15\epsilon}{aD} \quad \ldots (4)$$

where D is the crystallite size as determined by equation 1, a is the lattice dimension, and ϵ is the lattice microstrain. In the highly doped BTS ceramic, the dislocation density drops from 0.00053 in the undoped BTS to 0.00043. These variations in dislocation density affect the material's mechanical strength, dielectric behaviour, and ferroelectric performance. A lower dislocation density indicates a more ordered and stable crystal lattice, which enhances electrical properties and structural integrity.

3.4 Williamson-Hall (W-H) Plots of BTS and Gd-doped BTS Ceramics

Despite its broad applicability, the Debye-Scherrer method often fails to provide a reliable estimate of

Table 3 — Crystallographic characteristics derived from the X-ray diffraction analysis of the synthesized samples

Parameters	Samples			
	BTS (x=0.0)	G25 (x=0.025)	G50 (x=0.050)	G75 (x=0.075)
Crystallite Size D(nm) (±1)	26	27	27	28
Stacking Fault α (± 0.00001)	0.00235	0.00215	0.00218	0.00213
Lattice Microstrain ϵ (± 0.00001)	0.00343	0.00318	0.00320	0.00313
Dislocation Density ρ (± 0.00001)	0.00053	0.00044	0.00044	0.00043

crystallite size when X-ray diffraction peak broadening arises from factors other than finite crystallite dimensions. In particular, the Scherrer equation neglects contributions from atomic-scale strain and lattice distortions, which can cause a systematic underestimation of crystallite size. The Williamson-Hall (W-H) approach accounts for the effects of inhomogeneous microstrain on diffraction peak broadening and provides an accurate estimate of the average crystallite size, which was used to overcome these limitations. In such a method, the total peak broadening β, after instrumental effects correction, is separated into those components caused by size and strain[31], enabling the simultaneous estimation of both crystallite dimensions and lattice microstrain.

$$\beta = \beta_{size} + \beta_{microstrain} \quad \ldots (5)$$

Lattice defects and structural distortions introduce internal strain in the crystal, leading to peak broadening that can be quantitatively evaluated as;

$$\beta_{microstrain} = 4\varepsilon\, tan\theta \quad \ldots (6)$$

where ε denotes the microstrain produced in the crystal structure, and θ is the peak position in radians. So,

$$\beta = \frac{K\lambda}{D_{WH}\, Cos\, \theta} + 4\varepsilon\, tan\theta \quad \ldots (7)$$

On rearranging Eq. (7), it will become

$$\beta\, Cos\, \theta = \frac{K\lambda}{D_{WH}} + 4\varepsilon\, Sin\, \theta \quad \ldots (8)$$

Equation (8) corresponds to a linear relation, where the slope ε provides a measure of the lattice microstrain, while the intercept ($k\lambda/D_{WH}$) is used to calculate the crystallite size. Fig. 3 illustrates the Williamson–Hall (W–H) plots for all the synthesised ceramic samples. Origin software was employed for linear fitting, and the corresponding microstrain and crystallite size values extracted from the slope and intercept of these plots are summarised in Table 4. Figure 3 (a) shows a noticeable spread in the BTS data, reflecting an uneven particle size distribution and the presence of microstrain or structural defects within the sample[32]. The microstrain decreases on the introduction of gadolinium doping in the BTS lattice from 2.31 to 1.19 for the G75 sample. In addition to this, there is a decrease in crystallite size values from 52.12 nm to 44.15 nm for the G25 sample. But again, a further increase is observed with increasing gadolinium content. In low-doped samples, the presence of ions acts as a barrier to the growth of the

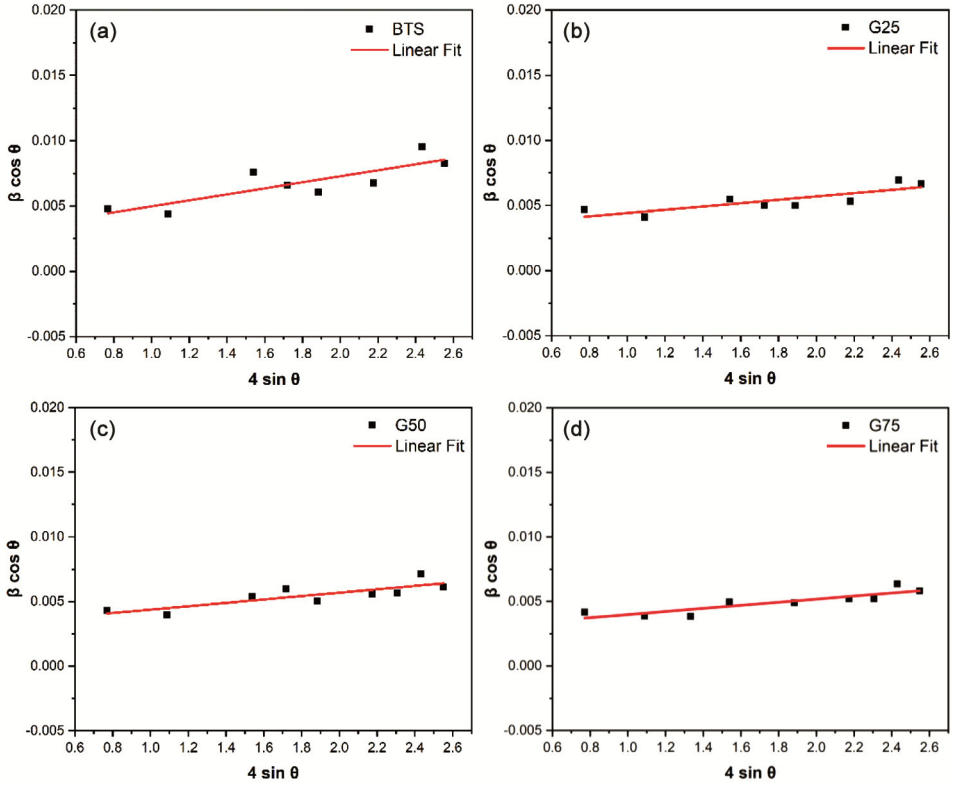

Fig. 3 — The Williamson–Hall (WH) plots for all the synthesized samples

Table 4 — The microstrain and crystallite size derived from W–H plots and the corresponding grain size determined from FESEM micrographs

Sample Name	Crystallite Size D_{WH}(nm)	Microstrain ε_{WH} (10^{-3})	Grain Size (μm) (± 0.001)
BTS	52.12	2.31	0.721
G25	44.15	1.28	0.387
G50	45.30	1.31	0.372
G75	49.69	1.19	0.289

grains. The lattice is unable to accommodate the ions easily. This results in a decrease in crystallite size despite partial strain relaxation. But with an increase in dopant concentration, ions are more readily accommodated in the lattice. This results in an increase in crystallite size and a decrease in microstrain. This again increases the crystallinity of the samples. The significant difference between the crystallite sizes estimated using the Scherrer formula (Table 3) and those values using the W–H method (Table 4) indicates the importance of microstrain concerning the broadening of diffraction peaks. This implies that the accuracy of estimating crystallite size using the Debye-Scherrer formula is reduced when diffraction peak broadening is due to factors other than crystallite size. The Scherrer equation often underestimates the actual crystallite size because it ignores strain effects, lattice distortions, and atomic-level contributions.

3.5 Electron Density Maps

Electron distribution maps were produced through the use of Full Prof Suite software's module name: GFourier. This was done to gain a clearer understanding of the anomalies within the crystal lattice. Through a Fourier transformation of the structure factors within an entire unit cell, this technique provides a clear picture of how atoms are organized inside[33]. These maps provide a clear visual representation of how valence electrons are localized within space. These maps have high accuracy in detecting even a tiny harmonic oscillation due to a subtle shift in an atom's position. The following is the expression for the atomic structure factor connected to the different diffraction reflections.

$$F_{hkl} = \iiint_{000}^{abc} \rho(x,y,z)\, e^{2\pi i(hx+ky+lz)}\, dxdydz \quad \ldots (9)$$

and the corresponding electron density at any point in the unit cell is obtained through the inverse Fourier transform of this relationship.

$$\rho(x,y,z) = \frac{1}{V} \Sigma\, F_{hkl}\, e^{-2\pi i(hx+ky+lz)} \quad \ldots (10)$$

This equation estimated the electron density.

The electron density 2D contour maps of all the synthesized samples were illustrated in Fig. 4 (a-d). On the contrary, its 3D Fourier maps are depicted in Fig. 5 (a-d), displaying periodic electron density concentrations around the atomic regions, along with lesser densities in the regions separating the atoms, thereby highlighting the electron distribution around the crystal structure.

These maps are sensitive enough to trace the subtle oscillations caused by slight variations in atomic positions. With increasing Gd^{3+} concentration, the distribution of electron densities becomes more smeared, suggesting that Gd atoms introduce slight variations in interatomic distances and ionic surroundings. This small-scale lattice adjustment gradually blurs the boundaries between areas of high and low electron density. At the same time, the overall periodicity and integrity of the crystal lattice remain intact, demonstrating that Gd acts as a local structural modulator rather than disrupting the fundamental framework.

3.6 FESEM

The morphological characteristics of the sintered samples were examined using high-resolution Field Emission Scanning Electron Microscopy (FESEM) to gain insight into grain evolution in the prepared materials. To achieve the best possible image quality and reliable microstructural analysis, all synthesised samples had to be prepared as pellets and coated with a thin gold layer before analysis. Figure 6 presents the FESEM micrographs of all synthesized samples recorded at a magnification of 30k. A detailed FESEM analysis was carried out to examine the microstructural properties of the samples, and the average grain size was quantified using ImageJ. The grain size was analysed by taking 3-4 points per grain at random orientations. Figure 7 presents the grain size distribution histograms for all synthesized samples. The undoped BTS ceramic exhibits a broad grain size distribution spanning approximately 0.2–1.6 μm, with an average grain size of 0.721 μm. With increasing dopant concentration, the distribution gradually narrows, indicating a more controlled and regulated grain growth process.

The microstructure analysis indicates that the grains are evenly distributed and have sharp boundaries. For the pure BTS ceramic, the average grain size was 0.721 μm. With the introduction of gadolinium into the BTS lattice structure, there is a

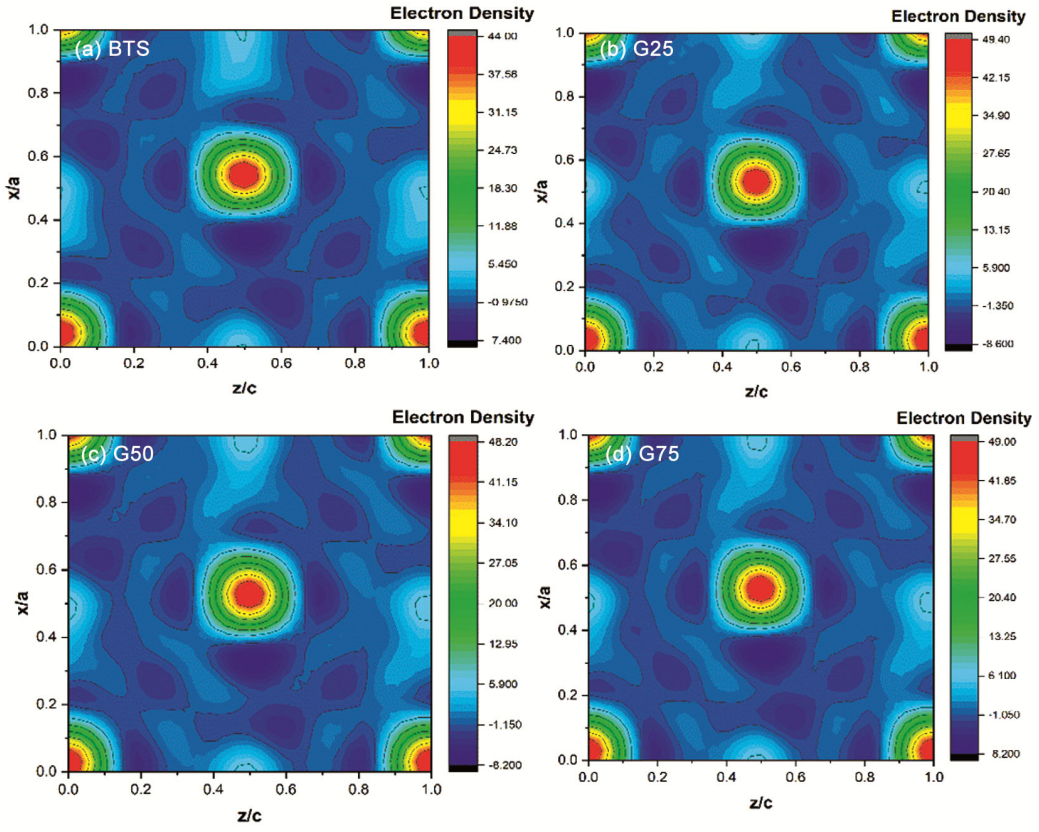

Fig. 4 — (a-d) Electron Density 2D Contour Maps for BTS, G25, G50 and G75 samples

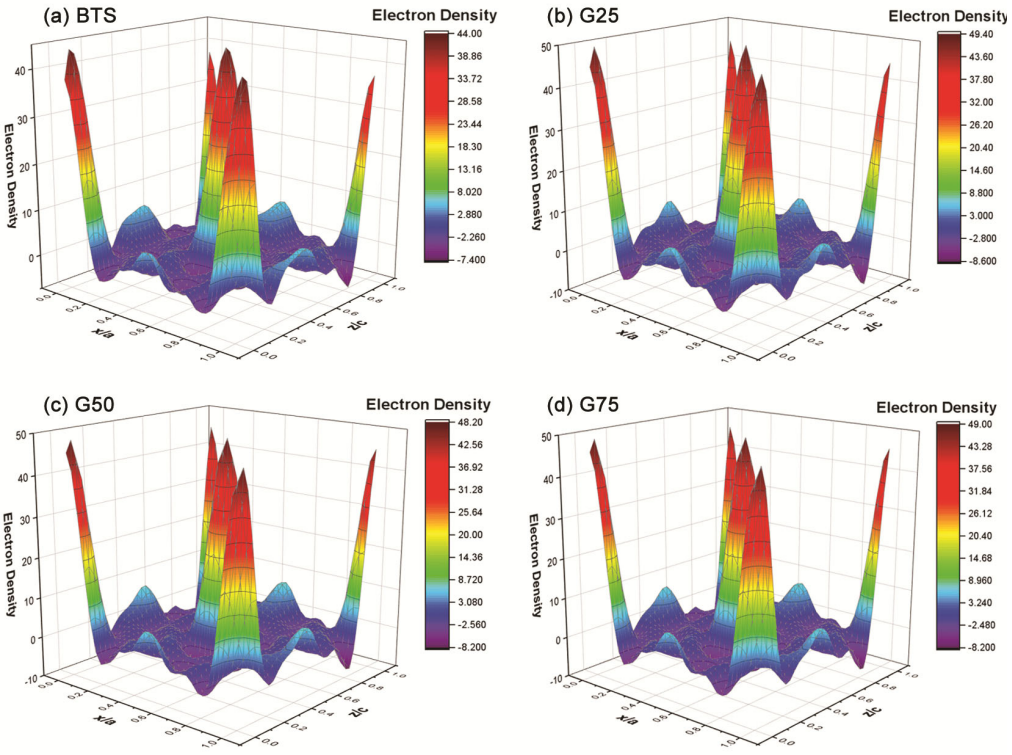

Fig. 5 — (a-d) 3D Fourier maps of electron density for BTS, G25, G50 and G75 samples

reduction in grain size to 0.387 µm for the G25 group. The reduction in grain size is contributed by the impurity drag mechanism, whereby the dopant ions are segregated at grain boundaries and interact with the migrating boundaries, producing an inhibiting force, which decreases grain boundary mobility and hinders grain growth[34]. With an increase in the concentration of gadolinium, there is a reduction in grain size to 0.372 µm and 0.289 µm for the G50 and G75 samples, respectively, because of the inhibitive nature of the $Gd_2Ti_2O_7$ type secondary phase[23,35]. The average grain size values are summarized in Table 4. Thus, it can be concluded that the concentration of gadolinium has a profound influence on grain growth as well as overall development during the evolution of the ceramic microstructure.

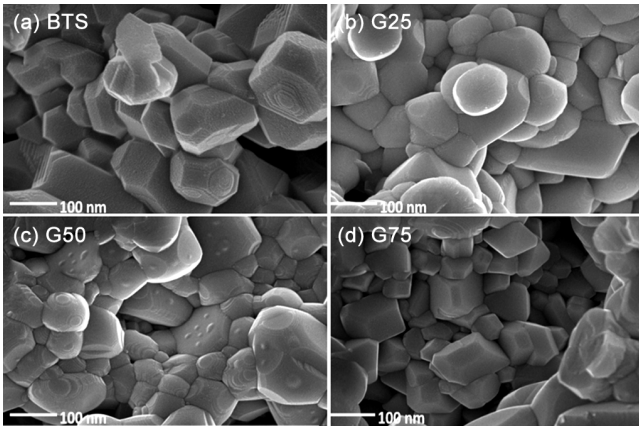

Fig. 6 — (a-d) FESEM micrographs for BTS, G25, G50 and G75 samples

Energy-dispersive spectroscopy (EDS) was performed on the Gd^{3+}-doped BTS ceramic samples to analyze their compositional purity and thus verify the appropriateness of the dopant ions incorporation. The principal constituent elements and their corresponding characteristic peaks are presented in Fig. 8 (a–d). From the EDS spectrum of the undoped BTS ceramic, the presence of Ba, Ti, Sn, and O is confirmed, with no impurity peaks, thus confirming its successful synthesis and high compositional purity. The Gd-doped samples (Fig. 8 b–d) exhibit characteristic peaks at the positions corresponding to Gd^{3+}, thus confirming the effective incorporation of gadolinium ions within the BTS perovskite lattice. In addition, the distribution of all elements is homogeneous, suggesting homogeneous Gd^{3+} incorporation within the lattice and, hence, uniform material performance. Summing up, the EDS results confirm the BTS ceramics are free from impurities and verify the effectiveness of the Gd^{3+} doping process.

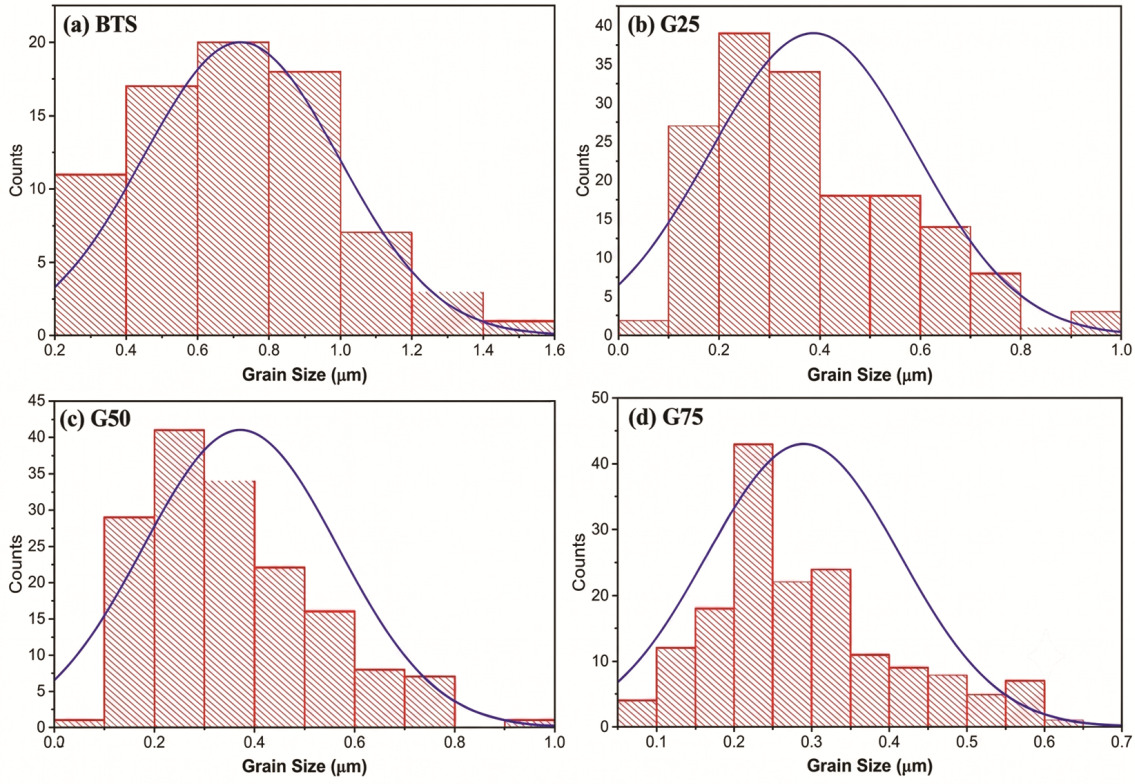

Fig. 7 — (a-d) Grain size distribution histograms for all the synthesized samples

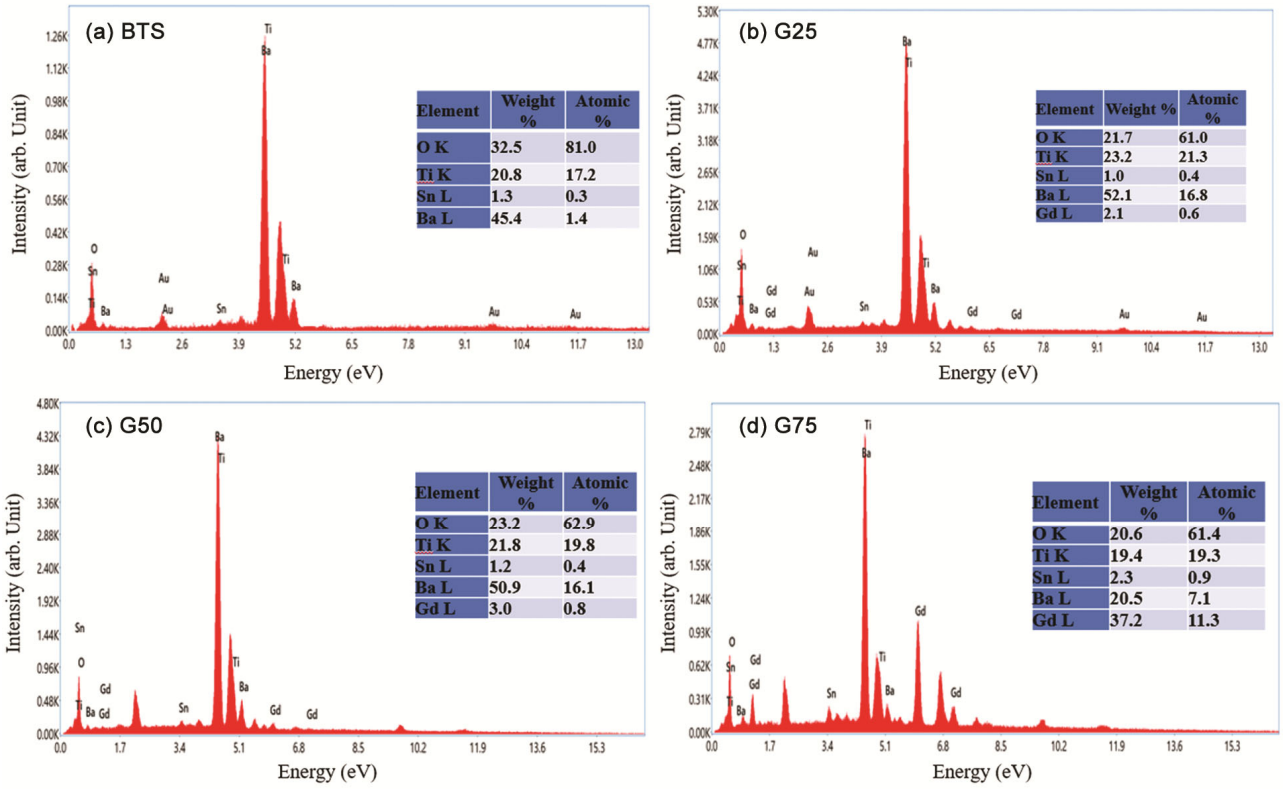

Fig. 8 — (a-d) Energy Dispersive X-ray Spectroscopy (EDS) spectra for all the synthesised samples

3.7 FTIR Spectroscopy

Fourier Transform Infrared (FTIR) Spectroscopy is a powerful vibrational spectroscopic tool employed to identify the functional groups and bonding environments of a material[36]. It relies on the detection of the absorbance of infrared photons of different frequencies, as different materials exhibit distinctive vibrational modes when irradiated with incident infrared photons. Such absorptions are exhibited by different frequencies and constitute the spectral fingerprint of the material or compound[37]. The FTIR spectra corresponding to all the synthesised samples are shown in Fig. 9. The principal absorption bands at 555 cm^{-1} and 652 cm^{-1}, attributed to the metal-oxygen vibrations, Ti–O vibrational mode[38]. The absorption band at 1437 cm^{-1} indicates the presence of surface carbonate (CO_3^{2-}), even though the XRD pattern (Fig. 1 (a)) shows no evidence of residual carbonate phases. Two factors could account for this observation. One possibility is that traces of the barium carbonate precursor remained unreacted and persisted on the surface in an amorphous form, which XRD would not detect. However, since the samples were calcined at 1250 °C for 3h, well above the ≈800 °C decomposition temperature of barium carbonate, the likelihood of unreacted precursor is minimal. A more plausible explanation is that the BTS surface readily interacts with atmospheric CO_2, leading to the formation of surface carbonates detectable in the FTIR spectrum; this peak disappears in the Gd^{3+} samples. The FTIR spectra of the gadolinium-doped samples become progressively flatter, eventually approaching linearity.

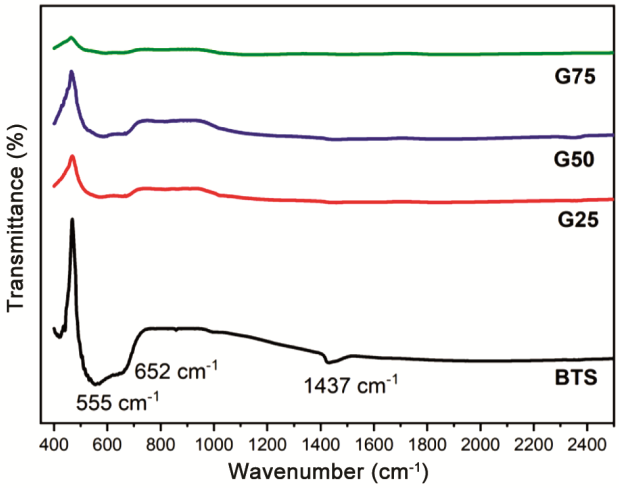

Fig. 9 — FTIR spectra for all the synthesized samples

These findings show that as Gd concentration increases, the characteristic BTS absorption peaks are

reduced or broadened. This is because the inclusion of Gd affects the local environment of Ti-O bonds. This could occur through variations in Ti-O bond lengths or the presence of oxygen vacancies. There is a slight change in the positions of the absorption peaks, too. It is evident that a small amount of Gd^{3+} ions occupies the B-site position[39]. This trend is consistent with the observations from the XRD analysis of pyrochlore phase formation, indicating good agreement between the spectroscopic and diffraction results.

Overall, the FTIR spectroscopy data support the qualitative preservation of the Ti–O metal-oxygen fundamental vibrational pattern in the BTS structure and provide well-detectable spectroscopic evidence of the Gd^{3+} ion incorporation. The gradual band flattening and widening, accompanied by a weak shift in positions, indicate that the local structure around Ti–O changes due to the effect of Ti–O bond length variations and the formation of defects (oxygen vacancies), as well as the onset of the occupation of the B-sites by a portion of the Gd^{3+} ions. The disappearance of the surface carbonate band after the addition of Gd, in addition to the agreement of the FTIR data behaviour and the pyrochlore structure formation suggested by the XRD data, emphasize the high structural sensitivity of the vibrational spectroscopy to the structural changes caused by the addition of the Gd ions.

3.8 Raman Spectroscopy

Raman spectroscopy was utilized to study the structural characteristics of the synthesized powders. The XRD findings were also verified using the technique. The technique's high structural sensitivity makes it useful for studying structural phase transformations, lattice disorder, and secondary phases in oxide materials. In addition to the structural characteristics, the technique provides detailed information on the crystallite symmetry, octahedral tilting, and characteristic modes. Figure 10 illustrates the normalized Raman spectra of the Gd-doped BTS ceramic samples measured at room temperature in the wavenumber range of 20-1000 cm-1. The graph shows the characteristic Raman peaks at 85 cm^{-1}, 243 cm^{-1}, 305 cm^{-1}, 515 cm^{-1}, 720 cm^{-1} and 830 cm^{-1}. Long-range electrostatic interactions split all A_1 and E vibrational modes into transverse optical (TO) and longitudinal optical (LO) components.

The soft mode corresponding to the structural phase transition, i.e., the $E(TO_1)$ mode, occurs at wavenumbers below[40] 100 cm^{-1}. The Raman band at 243 cm^{-1} is assigned to vibrations of Ti-O bonds. Conversely, the sharp bands at 515 and 720 cm−1 correspond to Ba-O vibrations. The sharp peak observed at 305 cm^{-1}, corresponding to the [B_1, E(TO+LO)] modes, is related to non-centrosymmetric areas created because of the Ti atom displacement in TiO_6 octahedral. This behaviour reflects the inherent structural distortion characteristics[41]. The asymmetric, broad peak around 515 cm^{-1} is identified as the $A_1(TO_3)$ mode. This particular band is derived from the motion between the Ti-O_1 entity and the atoms of O_2 and O_3. In this context, O_1 denotes the face-centered oxygen positioned along the c-axis, which is extended in the orthorhombic phase, whereas atoms O_2 and O_3 lie along the a-axis and b-axis, respectively[42]. This band progressively shifts toward higher wavenumbers with increasing gadolinium concentration in the synthesized samples. The peak observed at 720 cm^{-1} is attributed to the [$A_1(LO)$+ E(LO)] mode, $A_1(LO)$ arises from phonon propagation along the c-axis. In contrast, the E(LO) mode originates from phonon propagation within the ab-plane and is indicative of short-range polar ordering[38,43].

An additional Raman band was observed at around 830 cm^{-1}, with its intensity increasing with increasing Gd^{3+} concentration. This high-frequency mode (above 700 cm^{-1}) is commonly attributed to vibrational features associated with oxygen displacement and is often linked to the presence of oxygen vacancies. A similar band was reported by other researchers on doping different rare earth elements like Nd^{3+}, La^{3+}, Gd^{3+} in $BaTiO_3$[41,43,44]. The mismatch in ionic radii among Ba^{2+}, Ti^{4+}, and Gd^{3+} ions induces changes in

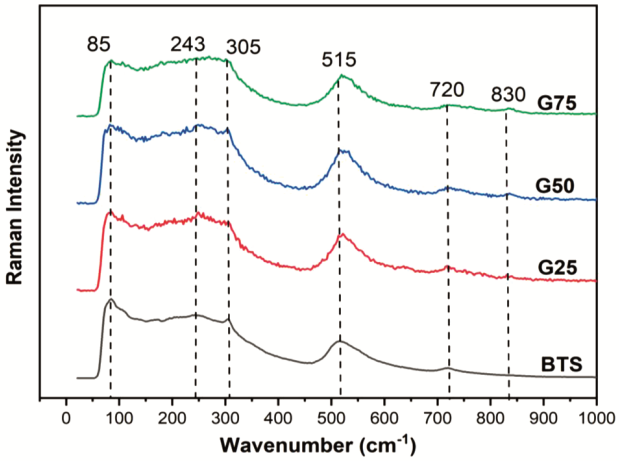

Fig. 10 — Normalized Raman spectra for Gd doped $Ba_{1-x}Gd_x$ $Ti_{0.965}Sn_{0.035}O_3$ (x = 0.00, 0.025, 0.05, 0.075) recorded at room temperature

the unit cell volume of the perovskite structure, as evidenced by the XRD results, indicating internal deformation or distortion of the TiO_6 octahedral. Such octahedral distortion has been reported to give rise to high-frequency Raman bands near 830 cm^{-1} known as raman charge effect[45]. Additionally, earlier studies have shown that the excess positive charge introduced by donor Gd^{3+} ions is compensated by the formation of cation vacancies, particularly barium vacancies, in Gd-doped $BaTiO_3$. The presence of Gd^{3+}–barium vacancy defect pairs can also contribute to Raman bands observed around 830 cm^{-1}. Notably, this extra band appeared only when the Gd^{3+} content exceeded 0.05, which is consistent with the emergence of the secondary $Gd_2Ti_2O_7$ phase, as also confirmed by the XRD analysis[43].

4 Conclusion

$Ba_{1-x}Gd_xTi_{0.965}Sn_{0.035}O_3$ (x = 0.00, 0.025, 0.05, 0.075) ceramics were successfully synthesized by the conventional solid-state reaction route, and their structural and microstructural evolution was systematically established. Gd incorporation was found to significantly refine the structural quality of $BaTi_{0.965}Sn_{0.035}O_3$, as evidenced by the reduction in lattice strain, stacking-fault probability, and dislocation density extracted from X-ray line-profile analysis. The sharp, well-resolved diffraction peaks and the absence of secondary phases at low Gd contents indicate that Gd^{3+} is effectively accommodated within the BTS perovskite lattice up to its solubility limit. Beyond this limit, the emergence of a pyrochlore-type secondary phase in the G50 and G75 compositions indicates the onset of phase segregation at higher Gd loadings.

Rietveld refinement of the XRD results indicates the dominant phase maintains a single-phase orthorhombic perovskite structure with space group Amm2. The 2D electron density maps of the structure, as well as 3D Fourier electron density maps generated with the GFourier module, confirmed an apparent periodicity in the electron density, with a subtle rearrangement of the structure around the incorporated Gd^{3+} ions. The observed grain refinement in FESEM microscopy indicates a substantial reduction in grain size from 0.721 μm to 0.289 μm, largely due to solute drag and the formation of a secondary phase. The energy-dispersive spectroscopy results verify the elemental composition of the synthesised samples, providing clear evidence of the incorporation of gadolinium ions into the lattice. Additionally, Raman spectroscopy reinforces the structural conclusions drawn from XRD and FTIR, providing complementary evidence of secondary-phase formation and lattice alteration.

Taken collectively, these results show that Gd doping provides an effective means to modify the crystal lattice, defects, and bonding environment in BTS ceramics, with the perovskite structure retained at least up to moderate doping concentrations. The structural insights gained offer a clear basis for further refinement of composition and processing parameters in future investigations and provide a robust platform for advanced dielectric and ferroelectric studies, highlighting Gd-modified BTS as a strong lead-free candidate for high-performance capacitors, actuators, sensors, and energy storage devices.

References

1 Smolensky G, *J Phys Soc*, 28 (1970) 26.
2 Lather A S, Poonia K, Kundu R S, Ahlawat N & Nehra A, Futuristic Trends in Chemical, Material Sciences & Nano Technology, Vol 3, IIP Series (Fresno USA) 2024, 123-136.
3 Wei X & Yao X, *Mater Sci Eng B*,137 (2007) 184.
4 Lather A S, Poonia K, Kundu R S, Ahlawat N, Nehra A & Kaur S, *ECS J Solid State Sci Technol*, 12 (2023) 093013.
5 N Horchidan, A C Ianculescu, L P Curecheriu, F Tudorache, V Musteata, S Stoleriu, N Dragan, D Crisan, S Tascu & L Mitoseriu, *J Alloys Compd,* 509 (2011) 4731.
6 Xiaoyong W, Yujun F & Xi Y, *Appl Phys Lett*, 83 (2003) 2031.
7 Yasuda N, Ohwa H & Asano S, *Jpn J Appl Phys*, 35 (1996) 5099.
8 Bongkarn T & Khiawwangthong W, *Adv Mater Res*, 55 (2008) 181.
9 L Jin, J Qiao, L Hou, Y Tian, Q Hu, L Wang, X Lu, L Zhang, H Du, X Wei, G Liu & Y Yan, *Ceram Int*, 44 (2018) 21816.
10 Deluca M, Stoleriu L, Curecheriu L P, Horchidan N, Ianculescu A C, Galassi C & Mitoseriu L, *J Appl Phys*, 111 (2012) 084102.
11 Wang S, Tan T A, Lai M O & Lu L, *Mater Res Bull*, 45 (2010) 279.
12 Dun W X, Li Y L, Zheng Z S, Yan S H & Wang Y F, *Dig J Nanomater Biostructures*, 12 (2017) 1081.
13 Sayed O El, Battisha I, Lahmar A & El Marssi M, *World J Nano Sci Eng*, 11 (2021) 25.
14 Hwang J H & Han Y H, S*olid State Ionics*, 140 (2001) 181.
15 Naveed-Ul-Haq M, *Mater Today Commun*, 28 (2021) 1.
16 Ansari M A, James A R, Zimik K, Bokolia R, Kundu R S & Sreenivas K, *Appl Phys A*, 128 (2022) 1.
17 Poonia K, Singh A, Ahlawat N, Kundu R S & Nehra A, *Ceram Int*, 51 (2025) 33105.
18 Wang F M, Li Y L & Yan C L, *Dig J Nanomater Biostructures*, 19 (2024) 785.
19 Kumari M, Baraik N & Sarun P M, *J Alloys Compd*, 883 (2021) 160635.
20 Kumar S, Pritam A, Shrivastava V, Thakur O P & Luthra V, *J Adv Dielectr*, 15 (2025) 1.

21 Devecioglu L, Salak AN, Kröll E, Shvartsman V V & Lupascu D *C, J Am Ceram Soc*, 108 (2025) 1.
22 Poonia K, Singh A, Ahlawat N, Kundu R S & Nehra A, Futuristic Research Trends of 2025, IIP Series (Fresno USA), 2025, 549-555.
23 Jeong J, Lee E J & Han Y H, *Japanese J Appl Physics*, 44 (2005) 4047.
24 Singh A S, Poonia K, Kundu R S, Ahlawat N & Nehra A, *J Energy Storage*, 86 (2024) 110691.
25 Buscaglia M T, Viviani M, Buscaglia V, Bottino C & Nanni P, *J Am Ceram Soc*, 85 (2002) 1569.
26 Zhi J, Chen A, Zhi Y, Vilarinho P M & Baptista J L, *J Am Ceram Soc*, 82 (1999) 1345.
27 Makovec D, Samardžija Z & Drofenik M, *J Am Ceram Soc*, 87 (2004) 1324.
28 Lee E J, Jeong J & Han Y H, *Japanese J Appl Phys* 43 (2004) 8126.
29 Rani K, Ahlawat N, Pooja, Kundu R S, Saini D & Deepa, *Appl Phys A,* 130 (2024) 290.
30 Poonia K, Lather A S, Jangra S, Kundu R S & Nehra A, *Mater Today Proc*, (2023).
31 Lather AS, Poonia K, Kundu RS, Ahlawat N, Nehra A & Kaur S, *J Phys Conf Ser* 2663 (2023) 012024.
32 Tayade N T & Tirpude M P, *Bull Mater Sci*, 46 (2023) 20.
33 Kumar S, Kumari S, Kar M, Singh A, Pathak H, Borah J P & Kumar L, *J Phys Chem Solids*, 151(2021) 109928.
34 Alkathy M S, Goud J P, Ibrahim K E & Kassim H A, *J Ovonic Res*, 20 (2024) 513.
35 Wang J H H & Han Y H, *Jpn J Appl Phys*, 40 (2001) 676.
36 Lather A S, Poonia K, Kundu R S, Ahlawat N, Nehra A & Kaur S, *J Adv Dielectr*, 13 (2023) 2350028.
37 Lather AS, Poonia K, Kundu R S, Ahlawat N, Nehra A & Kaur S, *Process Appl Ceram*, 18 (2024) 29.
38 Kumar S & Luthra V, *J Phys Chem Solids*, 154 (2021) 110079.
39 Ganguly M, Rout S K, Woo W S, Ahn C W & Kim I W, *Physica B*, 411 (2013) 26.
40 Maslova O A, Yuzyuk Y I, Ortega N, A Kumar, R Katiyar & Svetlana Aleksandrovna Barannikova, *Mat Res*, 22 (2019) 1.
41 Yao Z, Liu H, Liu Y, Wu Z, Shen Z & Liu M, *Mater Chem Phys*, 109 (2008) 475.
42 Ganguly M, Rout S K, Park H Y, Ahn C W & Kim I W, *Phys express*, 3 (2013) 1-12.
43 Pablo J, Lara H, Pérez M, Raúl F, Hernández B & Antonio, J. *Mater Res*, 20 (2017) 538.
44 Kchikech M & Maglione M, *J Phys Condens Matter,* 6 (2017) 10159.
45 Lu D yong, Sun X yun & Toda M, *J Phys Chem Solids,* 68 (2007) 650.